HHS Public Access

Author manuscript

J Comput Chem. Author manuscript; available in PMC 2016 June 15.

Published in final edited form as:

J Comput Chem. 2015 June 15; 36(16): 1196–1212. doi:10.1002/jcc.23906.

Free Energetics of Carbon Nanotube Association in Aqueous Inorganic NaI Salt Solutions: Temperature Effects using All-Atom Molecular Dynamics Simulations

Shu-Ching Ou[a], **Di Cui**[a], **Matthew Wezowicz**[b], **Michela Taufer**[b], and **Sandeep Patel**[a],‡

[a]Department of Chemistry and Biochemistry, University of Delaware, Newark, Delaware 19716, USA

[b]Department of Computer and Information Sciences, University of Delaware, Newark, Delaware 19716, USA

Abstract

In this study we examine the temperature dependence of free energetics of nanotube association by using GPU-enabled all-atom molecular dynamics simulations (FEN ZI) with two (10,10) single-walled carbon nanotubes in 3 m NaI aqueous salt solution. Results suggest that the free energy, enthalpy and entropy changes for the association process are all reduced at the high temperature, in agreement with previous investigations using other hydrophobes. Via the decomposition of free energy into individual components, we found that solvent contribution (including water, anion and cation contributions) is correlated with the spatial distribution of the corresponding species and is influenced distinctly by the temperature. We studied the spatial distribution and the structure of the solvent in different regions: intertube, intra-tube and the bulk solvent. By calculating the fluctuation of coarse-grained tube-solvent surfaces, we found that tube-water interfacial fluctuation exhibits the strongest temperature dependence. By taking ions to be a solvent-like medium in the absence of water, tube-anion interfacial fluctuation also shows similar but weaker dependence on temperature, while tube-cation interfacial fluctuation shows no dependence in general. These characteristics are discussed via the malleability of their corresponding solvation shells relative to the nanotube surface. Hydrogen bonding profiles and tetrahedrality of water arrangement are also computed to compare the structure of solvent in the solvent bulk and intertube region. The hydrophobic confinement induces a relatively lower concentration environment in the intertube region, therefore causing different intertube solvent structures which depend on the tube separation. This study is relevant in the continuing discourse on hydrophobic interactions (as they impact generally a broad class of phenomena in biology, biochemistry, and materials science and soft condensed matter research), and interpretations of hydrophobicity in terms of alternative but parallel signatures such as interfacial fluctuations, dewetting transitions, and enhanced fluctuation probabilities at interfaces.

‡sapatel@udel.edu.

Keywords

Hydrophobic Association; Single-Walled Carbon Nanotube; Temperature Dependence; Ion Adsorption; Graphics Processing Unit (GPU)

INTRODUCTION

With the plethora of future applications of carbon nanotube materials rapidly being realized and exploited, the assembly and aggregation of hydrophobes are inherent in a wide variety of fundamental and industrial processes[1–9]. Modulating the self-assembly process (either preventing it or exploiting it to create extended structures) often requires the addition of co-solutes. How these additives influence the hydrophobic assembly, directly or indirectly, is the central issue to understanding/explaining considerable fundamental questions. In the case of single-walled carbon nanotubes (SWNTs), recent research has focused on preventing the assembly/aggregation of SWNTs in solution, by involving addition of surfactants or surfactant-like dispersants[1,2,10–12]. These additional molecules effectively present a barrier for close contact between SWNTs, thus affording some control of aggregation behavior.

On the other hand, inorganic ions have recently been found to present significant effects on regulating dispersing properties of carbon nanotubes or other hydrophobic solutes. Niyogi *et al.* reported that without adding any co-surfactant, the use of metal chloride salts leads to a reduction in internanotube interactions[13,14]. While considering hydrophobic interactions, it is proposed that the different spatial preference of ions around the hydrophobes is critical to the types of (in)stability conferred on the solutes in the self-assembly process[15]. Larger ionic charge density species may amplify the hydrophobic interaction between nonpolar solutes and show different effects with smaller ionic charge density species[16–18]. In a biological context, these specific ion effects such as those observed by Hofmeister[19–27] relating to the “salting-in” (increasing the solubility of proteins) and “salting-out” (antisolvent crystallization, precipitation crystallization) of proteins in aqueous electrolyte solutions of varying ionic species and concentrations have been pursued from theoretical, modeling, and experimental approaches for decades; studies continue to probe the fundamental phenomenology of this effect[15,20–22,25,26,28–52]. Horinek *et al.* investigated the free energetics for Na^+, Cl^-, Br^- and I^- to transfer from bulk aqueous solution to a hydrophobic self-assembled monolayer (SAM)-water interface in an infinite dilution[48] and reported that soft polarizable monovalent anions (I^- and Br^-) prefer to accumulate around the hydrophobic interface. Nelson and Schwartz examined the effects of ions taken from opposite ends of the Hofmeister series (F^- and SCN^-) on the dynamics of a hydrophobic probe molecule at the SAM-aqueous interface via single-molecule total internal reflection fluorescence microscopy[53] and revealed that the adsorption rate of the probe molecule to the SAM increased systematically in the presence of F^- anions, which are expected to increase hydrophobic interactions. Using the association of two model hydrophobic plates, Zangi *et al.* reported “salting-out” as being entropically-driven by ions with high charge density (the effect increasing with charge density)[35,41], and less polarizability, that form strong hydration complexes away from the hydrophobic surfaces, whereas “salting-in”, is caused by ions with

lower charge density, and greater polarizability, that exhibit preferential binding at the hydrophobic surfaces and stabilized by entropic or enthalpic effects.

The propensity of larger halide anions to the water-hydrophobe interface is consistent with the scenario of anions at liquid-vapor interfaces (which represent the limit of the most hydrophobic interface)[15,51,52]. Recent studies[54–59] have begun to consider differential perturbations of liquid-vapor interfacial fluctuations induced by different ions along with ionic surface affinities. It is observed that the surface stable (an)ions induce larger interfacial fluctuations compared to the non-surface active species, thus demonstrating a strong correlation between induced interfacial fluctuations and ion surface stability as observed from molecular simulations. Ou *et al.* traced these differences in induced interfacial fluctuations to the nature of the hydration environment around the ions; water molecules in the hydration shells of surface stable species are shown to be more dynamic and less persistent compared to those in proximity to the non-surface stable species. When approaching the liquid-vapor interfaces, coupling of local solvent around ions with solvent further away and near an interface leads to different perturbations of the interface by ions, and thus vastly different contributions to interfacial fluctuations, and ultimately surface stability. They also showed that the surface stability of I^- decreases as the temperature increases, as well as the corresponding induced fluctuations. In contrast, Cl^- shows no such temperature dependence either for surface stability or the induced fluctuations[56]; for this reason, we consider only I^- in the present study. Because of this implied connection of the behaviors of ions at ideally hydrophobic aqueous liquid-vapor interfaces, we seek to address effects of ions at other hydrophobe-water interfaces. We anticipate that similar qualitative trends and behaviors should arise in the hydrophobe context as observed at liquid-vapor interfaces.

The present study continues to probe the effects of simple inorganic salt solutions, sodium iodide (NaI), on the energetics of assembly in such systems, and provides a reference point from which to consider systems where salts are used in combination with larger dispersants (i.e., surfactants, polymers, etc.) in order to effect desired physical behaviors leading to desired physical properties and structures. Particularly, we are interested in the temperature dependence of the free energetics of association, and how the contributions of water and ions change with temperature, as well as the hydrophobe-solvent interfacial fluctuation. We hope to be able to explain the temperature dependencies within the context of our model invoking the spatial distribution of interacting species as a mode for conferring (de)stabilizing effects for association.

Furthermore, as an extension, we adopt the use of Graphical Processing Units (GPUs) as a new platform for molecular simulations of fully atomically resolved systems[60–69]. Specifically, we use GPU resources to extend the sampling times of our all-atom systems in order to compute well-converged potentials of mean force (vis-a-vis, free energies or reversible work) that require substantial sampling for statistical precision. We use current state-of-the-art algorithms for treatment of electrostatics and short-range dispersion interactions, in order to faithfully retain the quality of well-validated force fields in our studies.

This article is organized as followed. First we describe the force fields and computational details. In the next section we present our results in three topics. We consider potential of mean force for nanotube association and the contribution from system components along with the temperature dependence of this property. We continue with examining the density of water molecules and ions at the water-tube interface facing the water bulk, as represented by the local hydrogen bonding patterns and tetrahedrality. The profiles for the region between the nanotubes are discussed to explain the difference observed in potential of mean force. We further present our results of tube-water and tube-ion surface fluctuations. The last section concludes our findings and general discussion.

METHODOLOGY

Force Fields

Molecular dynamics simulations were performed using a custom-developed code, FEN ZI[70,71] on two GPU clusters, a local GPU cluster at the University of Delaware and a XSEDE GPU cluster called Keeneland (KIDS) at Oak Ridge National Lab. The local cluster includes 48 dual six-core compute nodes (576 cores), 96 Fermi S2070 GPU systems, four GPUs per node. The cluster utilizes both an Infiniband fabric and a Gigabit Ethernet interconnect. KIDS is a HP SL-390 (Ariston) cluster with Intel Westmere hex-core CPUs, NVIDIA 6GB Fermi NVIDIA M2070 GPUs, and a Qlogic QDR InfiniBand interconnect. The system has 120 nodes with 240 CPUs and 360 GPUs, three GPUs per node. GPUs provide substantial speed-up (up to 10X) and allow the scalable study of larger molecular systems compared to traditional many-core CPU-based clusters. We provided detailed performance comparisons of GPU-based MD simulations using Fen Zi versus CPU-based MD simulations using traditional codes such as CHARMM in our previous work[71,72]. Details of performance tests can be found in Reference[68,69,71,72].

We chose to run canonical ensemble (*NVT*) simulations using the geometry shown in Figure 1; the central simulation cell consists of two liquid-vapor interfaces. This geometry allows the solvent density to relax in response to the presence of the carbon nanotubes. With respect to calculation of potentials of mean force, to be discussed further below, the methodology adopted in this work has been shown to reproduce the results for large hydrophobe association free energetics using constant pressure molecular dynamics simulations[73]. Temperature was maintained at T = 300, 310, 320, 330, 340, 350 and 360 K using a Nosé-Hoover thermostat[74]. The simulation cell was rectangular with dimensions of L_x = 40 Å, L_y = 40 Å and L_z = 200 Å, in which z is the direction normal to the liquid-vapor interface. Two (10,10) single wall carbon nanotubes are parallel and oriented along the x-direction. The SWNTs are constructed with the Nanotube Modeler package[75]. Each (10,10) SWNT is comprised of 400 carbon atoms with the bond length of 1.421 Å [76]. The diameter (D) and the length (l) of each tube are 13.56 Å and 24.0 Å, respectively. Throughout the simulation the positions of all tube atoms were fixed. The Lennard-Jones (LJ) parameters of the tube atoms were ε = 0.0663 kcal/mol, R_{min} = 4.0195 Å; however, the interactions among carbon atoms on the same tube were excluded. The water-carbon interactions were fixed to be ε_{ij} = 0.1015 kcal/mol, R_{min} = 3.7793 Å. These parameters are adopted from previous studies[15,77], which have been validated to model hydrophobic effects in understanding the

nature of surface friction in nanoscale fluid transport. For two SWNTs in pure water, a bulk slab consists of 7000 water molecules, which are represented by the extended simple point charge (SPC/E) model[78]. To generate 3 m salt solutions, 736 water molecules were replaced randomly with 368 pairs of anions and cations (yielding a final system of 6264 SPC/E water molecules, 368 anions, 368 cations). The molar concentrations used throughout this work are only approximate concentrations since they depend on the actual physical volume of the solution, which fluctuates slightly in this system with liquid-vapor interfaces. The actual molality (moles of ion over the mass of water) is 3.255 mol kg^{-1}; we retain the approximate molar concentrations for convenience. In order to obtain the potential of mean force (PMF) as a function of the separation between two SWNTs, we define a collective variable (or order parameter), *d*, as the distance between the center axes of the tubes In this study we sample more than 50 separations/windows between 16.4 Å and 26.0 Å.

For SPC/E water, the LJ parameters are ε_{OO} = 0.1554 kcal/mol, R_{min} = 3.5537 Å and are assigned only to the oxygen atoms. Point charges of oxygen and hydrogen atoms are q_O = −0.8476*e* and q_H = +0.4238*e*, respectively. Ions were treated as non-polarizable particles with interaction parameters based on those by Fyta *et al.*[79] which have been shown to reproduce experimental solvation free energies and the osmotic coefficients. All the LJ parameters are summarized in Table 1.

The non-bond interactions were treated via the standard Lennard-Jones “12-6” potential

$$E_{\mathrm{LJ}}=\sum_{ij}\varepsilon_{ij}\left(\frac{R_{\min,ij}^{12}}{r_{ij}^{12}}-2\frac{R_{\min,ij}^{6}}{r_{ij}^{6}}\right) \quad (1)$$

The parameters of ion-tube and ion-water interactions were determined by the Lorentz-Berthelot combining rules:

$$\varepsilon_{ij}=\sqrt{\varepsilon_i\varepsilon_j},\qquad R_{\min,ij}=\frac{R_{\min,i}+R_{\min,j}}{2} \quad (2)$$

Lennard-Jones interactions were gradually switched off at interparticle distance of 12 Å, with a gradual switching between 10 Å and 12 Å using the switching function:

$$S(r_{ij})=\begin{cases}1 & r_{ij}\le r_{\mathrm{on}}\\ \dfrac{\left(r_{\mathrm{off}}^2-r_{ij}^2\right)^2\left(r_{\mathrm{off}}^2+2r_{ij}^2-3r_{\mathrm{on}}^2\right)}{\left(r_{\mathrm{off}}^2-r_{\mathrm{on}}^2\right)^3} & r_{\mathrm{on}}<r_{ij}\le r_{\mathrm{off}}\\ 0 & r_{ij}>r_{\mathrm{off}}\end{cases} \quad (3)$$

In considering the force field to use for this study, our philosophy is to attempt to apply models developed and validated to some degree based on considerations of the hydration free energy of ions in pure water. We believe that consideration of ionic solutions requires attention to this chemical aspect of the physics of these systems. We acknowledge that the

precise absolute values of hydration free energies are fraught with assumptions necessarily arising from the inseparability, in reality, of electroneutral anion-cation pairs. Furthermore, the nature of the water-hydrophobe interface is also critical when considering simulations of the nature presented here, and within this context, we have chosen force fields that, again, have been validated with the nature of this interface in mind.

Conditionally convergent long-range electrostatic interactions were treated using Particle Mesh Ewald (PME)[80] approach with a 40 × 40 × 200 point grid and $\kappa = 0.330$. SHAKE[81] was used to maintain the rigid geometry of each water molecule. Dynamics were propagated using a Velocity-Verlet integrator with a 1.0 fs timestep under 3D periodic boundary conditions. The sampling time for each window was at least 150 ns. Properties were calculated from all but the first 5 ns, which was treated as equilibration, resulting in more than 145 ns per window for data analyses. Details of performance tests of FENZI can be found in Reference[68,69]. Empirically, the performance can reach 6 ns per day using a single C2090 GPU for each simulation window.

Potential of Mean Force Calculation

The PMF for nanotube association following an order parameter that brings the parallel-oriented tubes from an large-separation, dissociated state to the associated/contact state is calculated directly from the average forces acting on a tube:

$$W(\xi) = -\int \langle F(\xi) \rangle \, d\xi \quad (4)$$

where ξ is the collective variable taken as the separation distance between the center of mass of the two carbon nanotubes. We consider the average of forces $\langle F(\xi) \rangle$ acting on each nanotube over the sampled configurations at each separation distance; the average force used in the integration is the average of the values for the two SWNTs after negating the forces acting on the CNT located in the negative *z*-region of the simulation cell. All profiles of the PMF are shifted such that $W(\xi_{\text{dissociated}}) = 0$ kcal/mol, therefore, the difference in PMF from dissociated state to the global minimum (the contact state) is defined as:

$$\Delta W_{\text{total}} = W(\xi_{\text{contact}}) - W(\xi_{\text{dissociated}}) \quad (5)$$

We can consider the total force acting on the nanotubes as well as the decomposition of the total force into constituent contributions:

$$\begin{aligned} \Delta W_{\text{total}} &= \Delta W_{\text{non-solv}} + \Delta W_{\text{solv}} \\ &= -\int \langle F_{\text{non-solv}}(\xi) \rangle \, d\xi - \int \langle F_{\text{solv}}(\xi) \rangle \, d\xi \end{aligned} \quad (6)$$

where the subscript stands for either solvent induced or non-solvent induced contribution. Since tubes are the only non-solvent component and being fixed throughout the simulation for each separation distance, the tube contribution to the PMF is identical in all systems, giving $\Delta W_{\text{non-solv}} = \Delta W_{\text{tubes}}$ as a constant. Therefore, any differences in the PMF for our systems are solvent (water and ions) driven. Considering the equivalence of the Gibbs and Helmholtz potentials by neglecting small ambient-condition P-V contributions to the former, ΔW_{solv} is then our Gibbs free energy change.

Hydrophobe-Solvent Fluctuation Analysis

From individual snapshots/configurations we can construct the coarse-grained instantaneous surface defined by Willard and Chandler[82]. Gaussian mass distributions are assigned to each water oxygen atom (or ion):

$$\Phi(\mathbf{r};\xi)=(2\pi\xi^2)^{-d/2}exp(-r^2/2\xi^2) \quad (7)$$

where r is the magnitude of $\mathbf{r}$, ξ is correlation length, and d stands for dimensionality. We use correlation length = 3 Å, which is roughly the size of a single water molecule in the bulk, to assign the Gaussian mass to each water oxygen. However, unlike the water, the total number of ions is less, as a result we need to consider a larger correlation length (6 Å) to render the coarse-grained surface (further validation of the choice of 6 Å is included in supporting information). At space-time point $\mathbf{r}$, t, we have the coarse-grained density as

$$\overline{\varrho}(\mathbf{r},t)=\sum_i \Phi(|\mathbf{r}-\mathbf{r}_i(t)|;\xi) \quad (8)$$

The interface is then determined as the $(d-1)$-dimensional manifold with a constant value c. In the case of liquid-vapor interface, the surfaces are often orthogonal to an normal vector (z-vector), coordinate (x, y, z) for each grid points in space is set up and the surface is obtained as the manifold by setting $\varrho(x, y, z) = \varrho_{bulk}/2$ (based on the usual definition of Gibbs dividing surface). The mean surface of all the instantaneous surfaces is then described as the function $\langle h(x, y)\rangle$. Subtracting the mean values from the instantaneous $h_t(x, y)$, we obtain $\delta h_t(x, y)$ as surface height and the height fluctuations $\langle \delta h^2(x, y)\rangle$. Owing to the cylindrical geometry of nanotubes, we set up a series of (ρ, θ, l) (cylindrical) based grid points and treat ρ as the tube-water surface height, as shown in Figure 1d. ρ is radial distance of end point of the radius vector from the tube axis with the range 6.8 Å ≤ ρ ≤ 20 Å since we are interested in the tube-water surface outside the tube; θ is polar angle, which is defined as intersection angle between the radius vector and the positive y-vector with the range to ensure that only the hemisphere of interest is selected (facing the bulk: $0 \le \theta \le \pi$ or intertube region: $-\pi \le \theta \le 0$); l is the position along x-dimension with −11 Å ≤ l ≤ 11 Å. In practice, we set 66 × 18 × 22 grid points along (ρ, θ, l), which gives a resolution of (0.2 Å,10°,1 Å) in each dimension. The tube-water and tube-ion surfaces are defined as 3/4 bulk density of the corresponding species. We use a different constant value c here compared with liquid-vapor interface case to avoid the ambiguity during constructing the tube-solvent interface, as discussed in the Supporting Information. We note that in the current convention, instantaneous tube-solvent interface is then expressed as $h_t(\theta, l)$, mean surface as $\langle h(\theta, l)\rangle$, and the surface height fluctuation as $\langle \delta h^2(\theta, l)\rangle$.

RESULTS & DISCUSSION

Potential of Mean Force of CNT Association in NaI Solution

We start by considering the free energetics of nanotube association and its decomposition into enthalpic and entropic components to assess the relative contributions of these thermodynamic quantities. We show the PMFs of nanotube association in 3 m NaI solutions

at different temperatures in Figure 2a. The inset shows the minimum region of the PMF profiles. Numerical results (ΔW_{total}, as defined in Equation 5) are summarized in Table 2. We also include $\Delta W^b = W(\xi_{peak}) - W(\xi_{dissociated})$ as the value from the dissociated state to the first barrier (which is usually treated as the desolvation barrier for hydrophobic association process). The increase in stability, as represented with ΔW_{total}, is linear in temperature with a slope of −0.071 *kcal* mol^{-1} K^{-1}. This slope is consistent with the slope of stability for nanotubes in pure SPC/E (in the absence of ions, data not shown), which is not surprising since the water dominates the contribution to the PMF (will be discussed later). The barrier is seen to shift slightly toward larger ξ and exhibits a similar temperature dependence with a weaker slope −0.058 *kcal* mol^{-1} K^{-1}. Using two hydrophobic plates (diameter ~ 21 Å) with the same water model, Zangi and Berne[83] obtained a slope of −0.032 kcal mol^{-1} K^{-1} which is smaller than our result. Earlier, Mancera and Buckingham reported the aggregation of ethane in aqueous solution has a different dependence with temperature, in which they found at the intermediate 317 K ethane particles have the maximum tendency to aggregate [84]. Although not the main scope in this study, this might be related to the difference in solute size between ethane with the model hydrophobes in Zangi's and our work, since the thermodynamic driving force (enthalpic or entropic) is length-scale dependent[8,85].

We next consider the enthalpic and entropic components. In our system the volume change between the contact state and dissociated state is negligible, therefore the change in enthalpy (ΔH) is obtained as a difference in potential energy of the system at a particular tube-tube separation and that at the largest separation (dissociated state). To be consistent with ΔW_{solv}, we compute the total interaction energy between tubes and all other components of the system (which we consider the solvent—water, anions, and cations as relevant); this also includes interaction energy between elements of the solvent (water-ion, ion-ion, water-water). Since the tube-tube interaction is independent of the systems, we only look at the solvent induced enthalpic changes (ΔH_{solv}), which can be obtained by subtracting the direct tube-tube potential part from the overall enthalpic change. The entropic change is therefore determined from $-T\Delta S_{solv} = \Delta G_{solv} - \Delta H_{solv}$ [15,83]. Particularly, we plot ΔW_{solv}, ΔH_{solv} and ΔS_{solv} between dissociated state and contact state as functions of temperature in Figure 2b and c. The decorrelated uncertainties of ΔH_{solv} were obtained from block averages.[86].

We notice that values of ΔW_{solv} and ΔH_{solv} are positive for the temperature range in this study. Both Gibbs free energy change and enthalpic change are less repulsive at higher temperature, with a stronger slope/dependence for ΔH_{solv} than ΔW_{solv} to the temperature. This negative slope of enthalpic change with temperature is similar to that observed in the folding of proteins[87–89], although our system is under the condition of constant volume. ΔH_{solv} has a larger slope than ΔW_{solv} (as shown in Figure 2b), which indicates a compensation in entropic change. Since the tube atoms do not have any degree of freedom, ΔS_{solv} is essentially equal to solvent entropy. At high temperature, the ΔS_{solv} term is almost zero, consequently the association process is dominated by enthalpy; at low temperatures, ΔS_{solv} becomes 5 times larger and there is more entropic contribution to association. Similarly, Lüdemann *et al.*[90] studied the hydrophobic interactions of two methane-like particles in water and found that at 300 K the association is controlled by entropy, while the

internal energy takes over and dominates at high temperature. They reported that both enthalpy and entropy changes show crossover within the temperature range 300 K and 500 K. Here we will not argue whether the association process at the low temperature is dominated by enthalpic or entropic contribution, since the origin of that depends on the strength of solvent-tube interactions[83]. However, our main goal here is to reflect that the temperature dependencies of the three thermodynamic quantities in this work are similar to other studies at the nanometer scale qualitatively[83,91]. It implies that the parameters in this study are reasonable and also that there are underlying global similarities in the descriptions of atomic-level interactions.

Our next question is then, what is the temperature dependence of each component in the solvent? By using the same method in Reference[15,92] individual solvent-induced contributions to the PMF can be decomposed into:

$$\begin{aligned}\Delta W_{\mathrm{solv}} &= \Delta W_{\mathrm{water}} + \Delta W_{\mathrm{Na^+}} + \Delta W_{\mathrm{I^-}} \\ &= -\int \langle F_{\mathrm{water}}(\xi)\rangle \, d\xi - \int \langle F_{\mathrm{Na^+}}(\xi)\rangle \, d\xi - \int \langle F_{\mathrm{I}} - (\xi)\rangle \, d\xi \end{aligned} \quad (9)$$

The contribution from each component to the PMF is displayed in Figure 3; numerical values for individual component of ΔW_{solv} are listed in Table 2. As the major component to the solvent, the contribution to the PMF from water dominates the solvent contribution and disfavors nanotube association, which agrees with previous work using different nonpolar solutes[83,91,93–96]. It is also evident that the barriers and minima are largely affected by the water contribution. These barriers/minima are the consequences of solvent reorganization around the nanotubes and will be discussed later in this manuscript. Here we focus on the temperature effect to the free energetics. As the temperature increases, $\Delta W_{\mathrm{water}}$ becomes less positive/repulsive/destabilizing. On the other hand, $\Delta W_{\mathrm{I^-}}$ is negative/stabilizing at low temperature (which is consistent with our previous study[15]), but becomes destabilizing at high temperature. $\Delta W_{\mathrm{Na^+}}$ shows no significant difference among the temperatures ($\approx$ 1.3 kcal/mol).

We explain this difference of temperature dependence among the three species from the mechanistic point of view. The *z*-component of the total force from the individual species on all the tube atoms ($\langle F_{\mathrm{z},i}\rangle$) can be written as a function of the Cartesian positions (*x*, *y*, *z*) of the corresponding species. Then, by integrating over the length of nanotube, we obtain an average force that depends only on the *y* and *z* positions of the individual species as the integrated force map:

$$\langle F_{\mathrm{z},i}(y,z)\rangle = \left\langle \int_{-l'}^{l'} F_{\mathrm{z},i}{}'(x,y,z)dx \right\rangle \quad (10)$$

where $F_{\mathrm{z},i}{}'(x, y, z)$ corresponds to the sum of the forces applied on all tube atoms from given species *i* at position (*x*, *y*, *z*) (refer to Figure 6 in Reference[15]). However, the total force on the tubes is determined from the sum of the distribution/population of the force at the corresponding position, in other words, the density of the species, which is defined as:

$$\rho_i(y,z)=\int_{-l'}^{l'}\rho_i'(x,y,z)dx \quad (11)$$

where $\rho_i'(x,y,z)$ represents the number density of a given species *i* at position (*x*, *y*, *z*). We therefore have to multiply the density map of the species with the respective force map to explain how temperature results in different behavior among the three species.

We take water contribution as an example. In our system, tube atoms are neutral, therefore only van der Waals forces are considered for tube-water interactions. Shown in Figure 4a and b are $\langle F_{z,water}(y,z)\rangle$ at d = 16.4 Å and 19.4 Å. Again we emphasize that the force map is only related to how different tube separation affects the water spatial distribution, and is independent from the temperature. From the perspective of waters residing in the hemisphere facing the bulk solution, a negative value in the figure denotes that the net force in *z*-direction for the corresponding water at position (*y*, *z*) is repulsive and "pushes" the tubes to associate (stabilizing), while a positive value indicates an attractive net force that "pulls" the tubes apart (destabilizing). The opposite holds for waters within the inter-tube region. The figures are symmetrized by averaging forces from both tubes to increase the statistics since the tubes are equivalent about the center of the simulation cell. We can then categorize the "stabilizing water" and "destabilizing water" based on the spatial position of the water molecule. Since the force map is independent from the temperature, the difference in density-weighted forces between two temperatures is then determined by the difference of density maps. The difference of densities for water oxygen between 300 K (low temperature) and 360 K (high temperature), which can be written as $\rho_{i,300K}(y,z)-\rho_{i,360K}(y,z)$, are shown in Figure 4c and d, for the tube separation d = 16.4 Å and 19.4 Å, respectively. The difference of spatial density-weighted force map is then the product of panel a and c (or panel b and d), as presented in Figure 4e and f. In Figure 4a and b, the major difference is the strongly repulsive/destabilizing water band at the intertube region for d = 19.4 Å; on the other hand there is an excess of water in this intertube region at low temperature (as presented in Figure 4d). Meanwhile, due to more "destabilizing" water in the intertube region at 300 K, water contributes more repulsive/destabilizing forces in total. We include similar spatial maps for forces induced by the anions at 300 K and 360 K in the Supporting Information. We admit that without actually summing up the force, the current force map may not be quantitatively sufficient to explain the difference of solvent-induced PMFs; what we are suggesting is that the contributions from the waters/anions to the PMF for nanotube association are different and arise from the spatial distributions of each species at the different temperatures. This differences in spatial distribution for the bulk environment, in the vicinity of the nanotubes, and the intertube regions, are studied in the following sections to probe the origin of the temperature dependence of nanotube association.

Solvent Structure: Tube Center to Solution Bulk

In this section we will study the waters/ions residing in the hemisphere facing the bulk solution, as a reference/baseline for the behavior and structure of the solvent at different temperatures. We start with radial number density profiles of water molecules and ions about the tube. We restricted sampling for these profiles to a half cylinder on the side of the tube extending into the bulk solution. This prevents sampling in the intertube region where

the distributions will contain interference effects from the other tube. After each half cylinder is considered (for each tube) the symmetry of the two-tube system allows us to combine the sampling volumes into a full cylinder. Also, we limited the length of the sampling cylinder to $-l' \le x \le l'$ (l' = 11.0 Å), which is shorter than the tube length. Although being slightly reduced from the true length of the tube, it can avoid artifacts arising from the edge of the tubes. So the radial density profiles ($\rho(r)$) can be written as:

$$\rho_i(r) = \frac{N_i}{4\pi l' r dr} \quad (12)$$

where i is the atomic/molecular species, N_i is the corresponding number of species i within the region $r - dr/2$ to $r + dr/2$. Figure 5 shows the radial density profiles of water oxygen atoms and ions as a function of r which is relative to the center of the tube axes (at r = 0.0 Å).

In Figure 5a, we observe enhanced water density in the first solvation shell of the nanotubes which is consistent with earlier studies[97–99]. At higher temperatures, the structuring is reduced, though even up to 360 K the first shell retains a significantly enhanced density relative to the bulk. This effect may be attenuated with modified interaction potentials between water and hydrophobic moiety, but the essence of the physical effect will remain as long as physically relevant interaction energies/forces are incorporated in the force fields. We believe that the models for water-hydrophobe interactions applied here are well-tuned for this interface.

Figure 5b shows the density of I^- in the same regions corresponding to Figure 5a for water. We observe that the anion also exhibits enhanced interfacial density relative to the bulk; the temperature dependence is similar to that of water. This enhancement recapitulates previous studies showing the propensity of large anions to hydrophobic interfaces[48,100–102]. As the anion replaces water in the immediate vicinity of the tubes, the cation is forced to the next outer solvation layer, thus creating an electrical double layer in the immediate vicinity of the tube, as shown in Figure 5c. The enhancement of the cation is substantially lower than exhibited by the anion near the nanotube surface. The differences in anion and cation affinity at the hydrophobe interface are consequences of the differential hydration propensities; the smaller cation is well hydrated and prefers the bulk environment. Via experiments and simulations, previous work[54,56,103,104] showed that the total entropic contribution disfavors the presence of the ion at the hydrophobic interface consistent with the negative adsorption entropies of alkanes (from pentane up to octane) at an aqueous surface[105] suggesting that hydrophobic solvation might be significant in determining the affinities of ions near hydrophobic surfaces[59,106,107].

Furthermore, we observe that the cation is more probable to reside in the nanotube interior (r < 4.0 Å, intra-tube region) as demonstrated by the density profiles of Figure 5c. This is not surprising since the cation, being smaller, is also well solvated and does not lose its local hydration shell upon entering the intra-tube region. For this region, the average number of intra-tube water molecules ($\langle N_{\text{intra–tube,water}} \rangle$), anions ($\langle N_{\text{intra–tube,anion}} \rangle$) and cations ($\langle N_{\text{intra–tube,cation}} \rangle$) are summarized in Table 3. These values are calculated as direct

averages of the number of species in the tube normalized by the number of observations. Alternatively, though not done here, one can integrate the radial density profiles to obtain the equivalent value. Uncertainties included in the parentheses are determined from the standard deviations of $\langle N_{\text{intra–tube}} \rangle$. The average number of intra-tube water molecules is greatest at 300 K and follows the same temperature dependence as the first solvation shell; however, the average numbers of ions are low (about or less than one ion pair within the tube per snapshot) and they are not very sensitive to the system temperature. Similar to the interfacial propensities on the bulk solvent side of the tubes, we see that the anion, even when in the nanotube interior, displays enhanced density at the edge of the intra-tube volume, while the cation resides in the interior where it is well-solvated.

Recently, some studies found that the extent of air/water interfacial fluctuations induced by different ions correlates with the surface stability of the corresponding ion[54–58,108]. We next present the interface fluctuations of coarse-grained tube-water interfaces and tube-ion surfaces for the bulk sides of the tubes, to discuss the interfacial propensity of each species at different temperatures, as an application of the fluctuation analyses. The tube-ion surface was defined as the interface formed between the tube and the ions taken to be a solvent-like medium in the absence of water. This treatment is not unique as Feig and Pettitt also used ions as part of a solute's solvation shell[109]. Furthermore, since we use a high concentration of bulk anion, and considering the fact that the anion in this study prefers the tube-water interfacial region, analyses of the region in proximity to the interface by treating the ions as a continuous solvent-like medium places more validity on the approach. Ideally, because of the cylindrical symmetry of the tube, the surface fluctuation should be identical and independent of θ and l, except for the regions near the termini/edges of the tube. To represent the fluctuation values and prevent edge effects, we show the $\langle \delta h^2(\theta, l) \rangle$ as an average in the region $-5\ \text{Å} \leq l \leq 5\ \text{Å}$ and $85° \leq \theta \leq 95°$. The uncertainties were obtained via standard deviations. The results for tube-water and tube-ion fluctuations at different temperatures are shown in Figure 6a and b. A few salient features are noteworthy in this figure: (i) generally, the magnitude of tube-ion fluctuations is larger than tube-water fluctuations. (ii) All the solvent components show enhanced fluctuations as the temperature increases; however, in terms of the absolute magnitude, the difference (between 300 K and 360 K) in tube-I^- ($\approx 1.6\ \text{Å}^2$) is the greatest, followed by the difference in tube-water ($\approx 0.4\ \text{Å}^2$), and finally tube-Na^+ is rather modest ($\approx 0.3\ \text{Å}^2$). If we consider the relative magnitude of each component (normalized with the inherent fluctuation at 300 K), we have tube-water (53%) > tube-I^- (34%) > tube-Na^+ (4.6%). Therefore, the results suggest that tube-Na^+ shows basically no temperature dependence, while tube-I^- and tube-water are dependent upon temperature. Interestingly, this is consistent with what has been observed in the PMF and radial density profile.

We use the deformability/malleability of solvent shell to explain these features. From Figure 5a, the density ratio between the first peak (r = 10.1 Å) and the first minimum (r = 11.7 Å) of water is $0.095\ \text{Å}^{-3}/0.015\ \text{Å}^{-3} = 6.33$; from Figure 5b this ratio for I^- is $0.0031\ \text{Å}^{-3}/0.00095\ \text{Å}^{-3} = 3.26$; and for Na^+ this ratio is $0.0022\ \text{Å}^{-3}/0.0015\ \text{Å}^{-3} = 1.47$. The ratios demonstrate different manners in which the solvation shells of the nanotubes couple with the solvent component at the interface. Water retains the strongest, most unambiguous, well-

defined solvation shells, and does not support the intermixing with water from outer shells and therefore the tube-water interface is the least malleable. I^- holds the second strongest ordered solvation shells while Na^+ is the weakest, subsequently the tube-ion surfaces are more deformable. As the temperature increases, the ratios for water and I^- decrease (as highlighted in the insets), their malleabilities of solvation shells are increased, and consequently, the fluctuations arise. In the case of Na^+, the ratio between the first peak and the first minimum is insensitive to the temperature, hence no significant temperature dependence is observed.

Previously, we investigated the connection between the stability of a solute at an aqueous liquid-vapor interface and corresponding interface fluctuation. The fluctuation can be separated into inherent and solute-induced contributions. When temperature increases, the enhancement of inherent thermal water surface fluctuation rises, thus reducing the impact of any solvent structural perturbation induced by the solute[56]. This behavior accompanies the disappearance of an adsorption free energy minimum (i.e., interfacial free energy stability) of surface stable species near the interface. In this study, this behavior is shown as the reduction of the first peak of anion density (Figure 5b) as the temperature is increased.

As we suggested, the structure of solvation is important in explaining the temperature dependence of fluctuations and PMF; we consider the hydrogen bond network and geometric configurations at hydrophobic surfaces next. Specifically, we investigate hydrogen bonding numbers (average hydrogen bonds per molecule, $\langle N_{HB} \rangle$) and the angular tetrahedral parameters (q, to be defined further below) at various locations. Two water molecules were considered hydrogen bonded if the oxygen-oxygen distance is less than 3.5 Å and the HO ···O angle is less than 30°[15,73,110]. The average number of hydrogen bonds, normalized by the number of hydrogen bonds in the bulk for T = 300 and 360 K for the configuration d = 16.4 Å, are shown in Figure 7a as functions of r using the same cylindrical sampling volume that we used to compute the radial density profile. In aqueous salt solutions, due to the presence of ions, the bulk value of $\langle N_{HB} \rangle$ is less than the pure water case (about 3.5 hydrogen bonds per water molecule, refer to Reference[15]). The inset shows the numbers of hydrogen bonds per water molecule in the bulk at various temperatures in this study. The uncertainties were obtained via standard deviations. As the temperature increases, less hydrogen bonds are formed for bulk water. In the intra-tube region, water tends to hold more hydrogen bonds than water in the bulk region. This should not be surprising since on average only 1–2 ions are found in this region, the equivalent ion concentration is about half compared to the bulk. In the vicinity of the nanotubes, we found a slight enhancement followed by a depletion of hydrogen bonds; as the temperature elevates, the number of hydrogen bonds at the interface is reduced. Consider the deformation of hydrogen bond network as a result of lacking strong electrostatic interaction between hydrophobe and water: water-water interactions are therefore more important in shaping the orientation of water molecules[111]. Since the loss of hydrogen bonds is more likely to happen when there is another partner (i.e., another water molecule in our case) in the neighborhood to exchange the bond with, the location near the tube surface (which is liquid-vapor like) can promote the maximization of hydrogen bonding. However, the incompatibility of the tube surface with the tetrahedral network induces a distortion in the

donor-acceptor angle for the water at the interface than in the bulk[83]. With increased temperature, the rotational mobility of water increases. At high temperature, the water molecules in the bulk are correlated and therefore have to maintain a certain degree of tetrahedral network connectivity; however, the orientational preference of water near the tubes limits the ability to simultaneously rotate and maintain hydrogen bond connectivity. Shown in our supporting information, we observe a positive excess of hydrogen atoms in the vicinity of the tubes, indicating that the hydrogen atoms point closer to the tube and is consistent with this scenario.

We next apply the conditional tetrahedral parameter (q) introduced by Godec *et al.*[112] to describe the configurations of water near the nanotubes. For a tetrahedral configuration there are five points: the four vertices of the tetrahedron and the center. In a perfectly tetrahedral arrangement, all the angles between bonds hold the same value, and the cosine of this angle is −1/3. However, in the vicinity of the tubes, water molecules may not have four nearest hydrogen-bonded neighbors. Physically, at least two neighboring water molecules are necessary for a meaningful evaluation of tetrahedral order. The generalized form can be written as:

$$q_{\mathrm{i}}=1-\frac{1}{N(N-1)}\frac{9}{8}\sum_{j=1}^{N-1}\sum_{k=j+1}^{N}\left(cos\psi_{\mathrm{j,k}}+\frac{1}{3}\right)^{2} \quad (13)$$

where $\psi_{\mathrm{j,k}}$ is the angle subtended at the central water between the j_{th} and k_{th} bonds. N is the number of neighboring water molecules with $2 \le N \le 4$. The squaring ensures the contribution from each inter-bond angle is always greater than or equal to zero. The normalization factor is chosen so that $q_{\mathrm{i}} = 1$ when the configuration is perfectly tetrahedral (all the cosine values are −1/3); $q_{\mathrm{i}} = 0$ indicates the extreme non tetrahedral arrangement. The average tetrahedral order parameter, q, normalized by the corresponding bulk values (q_{bulk}) for T = 300 and 360 K with the configuration d = 16.4 Å, are shown in Figure 7b as functions of r using the same cylindrical sampling volume that we used to compute the radial density and hydrogen bond profiles. The inset shows q_{bulk} values as a function of temperature, the uncertainties were obtained via standard deviations. Consider the radius of the nanotube, which is roughly 6.8 Å, the tetrahedrality of water molecules shows slight enhancement, which extends up to 5.5 Å from the tube atoms. At 300 K, q reaches a maximum of 0.97, which is about $1.1q_{\mathrm{bulk}}$. q_{bulk} is not sensitive to temperature, gives only 0.95% difference between 300 K and 360 K, while $\langle N_{\mathrm{HB,bulk}}\rangle$ gives 7.26% difference between these two temperatures. Qualitatively, our results with temperature dependence are consistent with the experiment performed by Davis *et al.*[113]. The authors reported temperature-dependent Raman scattering measurements to investigate the hydrophobic hydration shells of linear alcohols. At low temperatures, the hydration shells were found to hold a hydrophobically enhanced water structure with greater tetrahedral order along with fewer weak hydrogen bonds than the surrounding bulk water. By increasing the temperature the structure is replaced by a less ordered structure with weaker hydrogen bonds than bulk water.

Solvent Structure: Intertube Region

Finally, we study the solvent structure of the intertube region. To investigate the behavior of water molecules and ions within the intertube region, we define a rectangular sampling volume as follows and illustrated in Figure 1b and c. The length (L) of the box is along the x-axis and identical with the cylinder used to sample for the radial density profiles, which makes L = 22.0 Å; the width (W) is along the z-axis and determined by subtracting from the tube separation (d) with the tube diameter (D = 13.56 Å). Finally, the height (H) equals $D - 2\,R_{\mathrm{min,OC}}$ and projects along the y-axis, with $R_{\mathrm{min,OC}}$ = 3.7866 Å based on Lorentz-Berthelot combining rules. The choice of this sampling region is not unique; we provide further analysis and an alternative scheme in the supporting information. Results are self-consistent using both sampling volumes. The average numbers of water oxygen atoms ($\langle N_{\mathrm{inter,water}}\rangle$), anions ($\langle N_{\mathrm{inter,anion}}\rangle$) and cations ($\langle N_{\mathrm{inter,cation}}\rangle$) in the rectangular box as functions of d are shown in Figure 8. Insets show focused view of the separation that there is a dramatic increase of $\langle N_{\mathrm{inter,water}}\rangle$ compared with other separations. As temperature increases, the number of intertube water is reduced. The plateaus in Figure 8a suggest the existence of stable solvation shells at particular tube separations, and are also found in other instances of hydrophobic association[91,114]. We plot the water oxygen density profile along z-dimension at 300 K and 360 K in Figure 9 to illustrate this behavior. Each $z \sim z + dz$ region has the same x and y-dimension length resulting in a sampling volume of $L \times H \times dz$. The second solvation shell of water only appears at the largest separation, therefore the total number of $\langle N_{\mathrm{inter,water}}\rangle$ is determined by the first solvation shell. At the same tube separation, the density of water at low temperature is substantially larger than the density at high temperature, which correlates with the water densities in the outer regions. Giovambattista *et al.* also found the same behavior for the water confined between two hydrophobic plates[115]. The effective hydrophobicity of the tube decreases as temperature decreases, consistent with the suppression of the vapor phase upon cooling. The numbers of anion and cations in the intertube region are not sensitive to the temperature, as shown in Figure 8b and c. We should point out that the difference of $\langle N_{\mathrm{inter,water}}\rangle$ in our system is very small (less than 3 water molecules at d = 22.0 Å); meanwhile, even at the largest separation, only 1.3 pairs of ions are observed, resulting in an equivalent concentration also about half compared to the bulk environment.

We next address the surface fluctuation for intertube region. Due to the scarcity of ions in this region, it is impractical to construct tube-ion interfaces. We therefore focus on the tube-water interface fluctuation. The results for tube-water fluctuations for various tube separations at 300 K and 360 K are shown in Figure 10. Refer to our supporting information for the results at other temperatures. At the dissociated state, we found $\langle \delta h^2(\theta, l)\rangle$ ranges from 0.6 to 0.65 Å^2 at all temperatures, which results from the analogous concentration/environment at this confined region. Also because of the lower local concentration in this region, we found a smaller $\langle \delta h^2(\theta, l)\rangle$ value relative to the fluctuation at the side facing the bulk (as shown with red dashed lines, along with the uncertainties, which are plotted as dotted lines). As the concentration of the solvent increases, surface tension increases and strengthens the hydrophobic effect. In our case, the reduction of ion concentration leads to less hydrophobicity and less induced interface fluctuations. In the supporting information,

we include our results of $\langle \delta h^2(\theta, l) \rangle$ of the sides facing the solvent bulk, at different concentration (0 m, 1 m, 3 m) of NaI aqueous solution.

It is worth noting that a crossover of $\langle \delta h^2(\theta, l) \rangle$ relative to the bulk side fluctuation happens between d = 22.0 Å and 23.0 Å (we do not consider the crossover between d = 21.0 Å and 22.0 Å due to the large uncertainties observed at all temperatures). First, at these separations, less than 0.5 pairs of ions are observed (refer to Figure 9b and c). Considering that there are ~ 20 water molecules in the intertube region, the "crossover" should be dictated by the water behavior. Again we use the "malleability" of solvation shell to explain this "crossover" of fluctuations. From Figure 9a, when d = 22.0 Å and 23.0 Å, the intertube densities are similar; but the ratio between the density peak and density minimum (i.e. z = 0 Å) are considerably different, as listed in Table 4. The shell "malleability" for d = 23.0 Å is therefore weaker than the case at d = 22.0 Å. As a consequence, the fluctuation for d = 23.0 Å is less. Recall that for the sides facing the solvent bulk, we have a ratio ~ 6.33 for the water solvation shell in the bulk side of the tube. This value 6.33 is between the ratios at d = 22.0 Å and d = 23.0 Å (both in low and high temperature scenarios), therefore a "crossover" behavior should not be surprising. This argument also holds when we compare the ratio at the same separation but different temperatures. At d = 22.0 Å, the ratio for 300 K (~ 2.76) is larger than the ratio (~ 1.94), therefore the former solvation shell is more rigid and holds a smaller fluctuation; meanwhile, at d = 23.0 Å, the ratio for 300 K (~ 22.76) is substantially greater. Consequently its corresponding fluctuation value is significantly lower.

We next address the hydrogen bonds and tetrahedrality of the water molecules as functions of z in the intertube region. The same sampling volume ($L \times H \times dz$) is used as for the analysis of intertube densities. The results of $\langle N_{HB} \rangle / N_{HB,bulk}$ and q/q_{bulk} at various tube separations at 300 K and 360 K are shown in Figure 11 and Figure 12. Usually, under the confinement of hydrophobes, the (CNT) walls do not form any hydrogen bonds with water molecules, and so the average number of hydrogen bonds per molecule in confined system is expected to be smaller than in bulk environment[116,117]. The addition of salts has little effect on the O-H and H-H structures but still distorts the arrangement of the water network[118]. Therefore the relatively lower concentration in the intertube region induces less hydrogen bond breaking (when d > 21.0Å), as shown in Figure 11. This concentration dependence of hydrogen bonding profile is consistent with the neutron diffraction data from monovalent ionic solutions reported by Mancinelli *et al.*[119]

For intertube water tetrahedrality, at small separation (d < 22.0 Å) all the $q(z)$ are smaller than the bulk value. When d = 22.0 Å (for both low and high temperatures) we observe that the largest $q(z)$ (at z = 0 Å) barely coincides with the bulk value. At d = 23.0 Å, strong enhanced q (even larger than the q_{bulk}) is discovered in the intertube region, indicating a highly-ordered structure of water molecules. Again, we use the idea of equivalent concentration in the intertube region to explain this behavior. From Figure 8, below the separation of 21 Å, the presence of ion is not found. There is also a limited amount of water in the intertube region to introduce tetrahedral structure. As the tube separation increases, this region allows the entry of ions, with a lower equivalent concentration relative to the bulk. The corresponding tetrahedral structure among water molecules is therefore less perturbed by the ions, in agreement with Galamba's results of tetrahedrality of water in

different concentration of aqueous salt solutions[120]. Another feature at d = 23.0 Å is that, considering q_{bulk} is insensitive to the temperature, we have $q(z)$ reduced for all values of z as temperature increases, suggesting that the local water structure becomes less ordered in this respect consistent with the temperature dependence reported by Giovambattista *et al.* using two hydrophobic plates[115]. However, due to the geometry of nanotubes and the resulting intertube environment, we observe no plateau region in our computed profile nor the wider profiles in $q(z)$ upon cooling[115,121].

CONCLUSION

In the preceding sections, we studied the effect of temperature on the interfacial properties of carbon nanotube assembly in 3 m NaI aqueous solution using GPU-enabled molecular dynamics simulations (FEN ZI). We examined the temperature behavior for the free energetics of two parallel single-walled carbon nanotubes by computing the potentials of mean force (PMF) between the contact state and dissociated state. Decomposition of solvent-induced PMF into changes in enthalpy and entropy suggests that all three thermodynamical quantities decrease with increasing temperature. At the highest temperature (360 K) in this manuscript, we found barely any entropic contribution to the free energetics. Further decomposition of PMF into each solvent component (water, I^- and Na^+) implies that as the dominant component, water contributes to the tube association in a less destabilizing manner as the temperature increases. I^- shows reversed trend, and Na^+ presents no dependence on temperature. From the mechanistic point of view, this difference in force contribution originates from differences in spatial distribution of the various system species. We investigated the spatial distribution and the structure of the solvent in different regions: intertube, intra-tube and the solvent bulk. For the bulk side of the nanotubes, by calculating the fluctuation of coarse-grained tube-solvent surfaces, we found that proportionally, tube-water interfacial fluctuation exhibits the strongest temperature dependence. Tube-I^- interfacial fluctuation also shows similar but weaker dependence to the temperature, while tube-Na^+ interfacial fluctuation shows no dependence in general. These characteristics are discussed via the malleability of their corresponding solvation shells. Hydrogen bonding profile and tetrahedrality of water arrangement are also computed to describe the structure of solvent at different temperatures. The analysis of hydrogen bonding in the vicinity of the nanotubes suggests an orientational preference of water molecules, implying a higher orientational order relative to the bulk water. In the intertube region, the hydrophobic confinement induces a relatively lower concentration environment (compared with bulk environment), therefore causing different behaviors depending on the tube separation.

In general, our work explained how association/dissociation between carbon nanotube materials can be modulated by controlling the temperature and inorganic additives. Essentially, the self-assembly strength is determined by the corresponding solvation structures. From the biological perspective, it is natural to connect the temperature and salt (concentration and type) dependencies to the studies of protein folding, micelle formations, protein-protein binding affinity and even protein-based materials[122]. Both experimentally and theoretically, there is already progress addressing temperature and solvent dependencies[123,124]; however, the heterogeneity of the biomolecular surfaces are much

more complicated than the simple hydrophobic models[125–130]. How these solvation structures behave, or how the malleability of the solvation shells can be evaluated as a response to the change of temperature and ionic strength are therefore ongoing avenues of inquiry.

Supplementary Material

Refer to Web version on PubMed Central for supplementary material.

Acknowledgments

The authors acknowledge support from the National Science Foundation (CAREER:MCB:1149802). Computational resources are acknowledged via support from National Institutes of Health (COBRE:P20-RR015588) in the Chemical Engineering Department at the University of Delaware and (COBRE: 5P20RR017716-07 and COBRE:1P30GM110758-01) at the University of Delaware, Department of Chemistry and Biochemistry. SP thanks N. Patel for fruitful discussion and encouragement for the duration of this work.

References

1. Frolov AI, Rozhin AG, Fedorov MV. Chem Phys Chem. 2010; 11:2612. [PubMed: 20629068]
2. Lin S, Blankschtein D. J Phys Chem B. 2010; 114:15616. [PubMed: 21050001]
3. Zelada-Guillen GA, Riu J, Duzgun A, Rius FX. Angew Chem Int Ed. 2009; 48:7334.
4. Zelada-Guillen GA, Riu J, Duzgun A, Rius FX. Angew Chem. 2009; 121:7470.
5. Chen RJ, Bangsaruntip S, Drouvalakis KA, Kam NWS, Shim M, Li Y, Kim W, Utz PJ, Dai H. Proc Nat Aca Sci. 2003; 100:4984.
6. Vaisman L, Wagner HD, Marom G. Adv Coll Int Sci. 2006; 128:37.
7. Moore VC, Strano MS, Haroz EH, Hauge RH, Smalley RE, Schimdt J, Talmon Y. Nano Lett. 2003; 3:1379.
8. Zangi R. J Phys Chem B. 2011; 115:2303. [PubMed: 21332173]
9. Ou SC, Patel S. J Chem Phys. 2014; 141:114906. [PubMed: 25240371]
10. Xu Z, Yang X, Yang Z. Nano Lett. 2010; 10:985. [PubMed: 20121238]
11. Angelikopoulos P, Beck H. J Phys Chem Lett. 2011; 2:139.
12. Wang J, Chu H, Li Y. ACS Nano. 2008; 2:2540. [PubMed: 19206290]
13. Niyogi S, Boukhalfa S, Chikkannanavar SB, McDonald TJ, Heben MJ, Doorn SK. J Am Chem Soc. 2007; 129:1898. [PubMed: 17253695]
14. Niyogi S, Densmore CG, Doorn SK. J Am Chem Soc. 2009; 131:1144. [PubMed: 19154177]
15. Ou S, Bauer BA, Patel S. J Phys Chem B. 2012; 116:8154. [PubMed: 22780909]
16. Collins KD. Biophy J. 1997; 72:65.
17. Baldwin RL. Biophys Jour. 1996; 71:2056. [PubMed: 8889180]
18. Vonhippel PH, Wong KY. Science. 1964; 7:577. [PubMed: 14163781]
19. Hofmeister F. Arch Exp Pathol Pharmakol. 1888; 24:247.
20. Kurutz JW, Xu S. Langmuir. 2001; 17:7323.
21. Neagu A, Neagu M, Dńr A. Biophy J. 2001; 81:1285.
22. Tadeo X, López-Méndez B, Castaño D, Millet O. Biophy J. 2009; 97:2595.
23. Kunz W, Henle J, Ninham BW. Curr Opin Colloid Inter Sci. 2004; 9:19.
24. Zhang Y, Cremer PS. Annu Rev Phys Chem. 2010; 61:63. [PubMed: 20055667]
25. dos Santos AP, Diehl A, Levin Y. Langmuir. 2010; 13:10778. [PubMed: 20361733]
26. Heyda J, Vincent JC, Tobias DJ, Dzubiella J, Jungwirth P. J Phys Chem B. 2010; 114:1213. [PubMed: 20038160]
27. Lund M, Vacha R, Jungwirth P. Langmuir. 2008; 24:3387. [PubMed: 18294017]
28. Petersen PB, Saykally RJ. Chem Phys Lett. 2004; 397:51.

29. Zhu S, Elcock AH. J Chem Theory Comput. 2010; 6:1293.
30. Thomas AS, Elcock AH. J Am Chem Soc. 2007; 129:14887. [PubMed: 17994735]
31. Collins KD, Washabaugh MW. Q Rev Biophys. 1985; 18:323. [PubMed: 3916340]
32. Horinek D, Serr A, Bonthuis DJ, Bostrom M, Kunz W, Netz RR. Langmuir. 2008; 24:1271. [PubMed: 18220430]
33. Ghosh T, Kalra A, Garde S. J Phys Chem B. 2005; 109:642. [PubMed: 16851057]
34. Godawat R, Jamadagni SN, Garde S. J Phys Chem B. 2010; 114:2246. [PubMed: 20146543]
35. Zangi R, Hagen M, Berne BJ. J Am Chem Soc. 2007; 129:4678. [PubMed: 17378564]
36. Collins KD. Methods. 2004; 34:300. [PubMed: 15325648]
37. Zhang Y, Cremer PS. Curr Opin Chem Bio. 2006; 10:658. [PubMed: 17035073]
38. Zhang YJ, Furyk S, Bergbreiter DE, Cremer PS. J Am Chem Soc. 2005; 127:14505. [PubMed: 16218647]
39. Chen X, Flores SC, Lim S, Zhang Y, Kherb J, Cremer PS. Langmuir. 2010; 26:16447. [PubMed: 20560589]
40. Levin Y, dos Santos AP, Diehl A. Phys Rev Lett. 2009; 103:257802. [PubMed: 20366288]
41. Zangi R, Berne BJ. J Phys Chem B. 2006; 110:22736. [PubMed: 17092024]
42. Wick CD, Xantheas SS. J Phys Chem B. 2009; 113:4141. [PubMed: 19014185]
43. Pegram LM, Record MT Jr. J Phys Chem B. 2007; 111:5411. [PubMed: 17432897]
44. Pegram LM, Record MT Jr. J Phys Chem B. 2008; 112:9428. [PubMed: 18630860]
45. Jungwirth P, Tobias DJ. Chem Rev. 2006; 106:1259. [PubMed: 16608180]
46. Jungwirth P, Tobias DJ. J Phys Chem B. 2002; 106:6361.
47. Jungwirth P, Tobias DJ. J Phys Chem B. 2001; 105:10468.
48. Horinek D, Netz RR. Phys Rev Lett. 2007; 99:226104. [PubMed: 18233302]
49. Horinek D, Herz A, Vrbka L, Sedlmeier F, Mamatkulov SI, Netz RR. Chem Phys Lett. 2009; 479:173.
50. Wick C, Kuo IW, Mundy CJ, Dang LX. J Chem Theory Comput. 2007; 3:2002.
51. Bauer BA, Ou S, Patel S. Phys Chem Chem Phys. 2012; 14:1892. [PubMed: 22231014]
52. Bauer BA, Ou S, Patel S. Chem Phys Lett. 2011; 527:22. [PubMed: 23136448]
53. Nelson N, Schwartz DK. J Phys Chem Lett. 2013; 4:4064.
54. Otten DE, Shaffer PR, Geissler PL, Saykally RJ. Proc Nat Aca Sci. 2012; 109:701.
55. Stern AC, Baer MD, Mundy CJ, Tobias DJ. J Chem Phys. 2013; 138:114709. [PubMed: 23534655]
56. Ou S, Patel S. J Phys Chem B. 2013; 117:6512. [PubMed: 23537166]
57. Ou S, Hu Y, Patel S, Wan H. J Phys Chem B. 2013; 117:11732. [PubMed: 24032752]
58. Ou S, Cui D, Patel S. J Phys Chem B. 2013; 117:11719. [PubMed: 23937431]
59. Ou SC, Cui D, Patel S. Phys Chem Chem Phys. 2014; 16:26779. [PubMed: 25372502]
60. Nguyen TD, Phillips CL, Anderson JA, Glotzer SC. Comp Phys Commun. 2011; 182:2307.
61. Phillips CL, Anderson JA, Glotzer SC. J Comp Phys. 2011; 230:7191.
62. Anderson JA, Lorenz CD, Travesset A. J Comp Phys. 2008; 227:5342.
63. Phillips CL, Anderson JA, Huber G, Glotzer SC. Phys Rev Lett. 2012; 108:198304. [PubMed: 23003097]
64. Anderson JA, Glotzer SC. 2013 arXiv:1308.5587.
65. Haque IS, Pande VS. J Comp Chem. 2009; 31:117. [PubMed: 19421991]
66. Stone JE, Vandivort KL, Schulten K. 2013:1–8.
67. Roberts E, Stone JE, Luthey-Schulten Z. J Comp Chem. 2013; 34:245. [PubMed: 23007888]
68. Schlachter, S.; Herbein, S.; Taufer, M.; Ou, S.; Patel, S.; Logan, JS. IEEE, eScience 9th International Conference; 2013. p. 116-123.
69. Schlachter S, Herbein S, Ou S, Logan JS, Patel S, Taufer M. IEEE Design & Test. 2014; 31:40.
70. Bauer BA, Davis JE, Taufer M, Patel S. J Comp Chem. 2011; 32:375. [PubMed: 20862755]

71. Ganesan N, Bauer BA, Lucas TR, Patel S, Taufer M. J Comp Chem. 2011; 32:2958. [PubMed: 21793003]
72. Taufer M, Ganesan N, Patel S. IEEE Computing in Science and Engineering (CiSE). 2013; 15:56.
73. Bauer BA, Patel S. J Phys Chem B. 2010; 114:8107. [PubMed: 20509706]
74. Nosé S. Mol Phys. 1984; 52:255.
75. JCrystalSoft. 2011. http://jcrystal.com/products/wincnt/index.htm
76. Dresselhaus, MS.; Dresselhaus, G.; Eklund, PC. Science of Fullerenes and Carbon Nanotubes. Academic Press; San Diego, CA: 1995.
77. Sendner C, Horinek D, Bocquet L, Netz RR. Langmuir. 2009; 25:10768. [PubMed: 19591481]
78. Berendsen HJC, Grigera JR, Straatsma TP. J Phys Chem. 1987; 91:6269.
79. Fyta M, Kalcher I, Dzubiella J, Netz RR. J Chem Phys. 2010; 132:024911. [PubMed: 20095713]
80. Darden T, York D, Pedersen L. J Chem Phys. 1993; 98:10089.
81. Ryckaert JP, Ciccotti G, Berendsen HJC. J Comp Phys. 1977; 23:327.
82. Willard AP, Chandler D. J Phys Chem B. 2010; 114:1954. [PubMed: 20055377]
83. Zangi R, Berne BJ. J Phys Chem B. 2008; 112:8634. [PubMed: 18582012]
84. Mancera RL, Buckingham AD. Chem Phys Lett. 1995; 234:296.
85. Huang DM, Chandler D. Proc Nat Aca Sci. 2000; 97:8324.
86. Flyvbjerg H, Petersen HG. J Chem Phys. 1989; 91:461.
87. Shimizu S, Chan HS. J Am Chem Soc. 2001; 123:2083. [PubMed: 11456842]
88. Prabhu NV, Sharp KA. Annu Rev Phys Chem. 2005; 56:521. [PubMed: 15796710]
89. Robertson AD, Murphy KP. Chem Rev. 1997; 97:1251. [PubMed: 11851450]
90. Lüdemann S, Abseher R, Schreiber H, Steinhauser O. J Chem Phys. 1997; 119:4206.
91. Choudhury N, Pettitt BM. J Phys Chem B. 2006; 110:8459. [PubMed: 16623532]
92. Ou S, Lucas TR, Zhong Y, Bauer BA, Hu Y, Patel S. J Phys Chem B. 2013; 117:3578. [PubMed: 23409975]
93. Li L, Bedrov D, Smith GD. J Chem Phys. 2005; 123:204504. [PubMed: 16351278]
94. Li L, Bedrov D, Smith GD. J Phys Chem B. 2006; 110:10509. [PubMed: 16722760]
95. Uddin NM, Capaldi FM, Farouk B. Polymer. 2011; 52:288.
96. Bauer BA, Ou S, Patel S, Siva K. Phys Rev E. 2012; 85:051506.
97. Raschke* TM, Levitt M. Proc Nat Aca Sci. 2005; 102:6777.
98. Galamba N. J Phys Chem B. 2013; 117:2153. [PubMed: 23360515]
99. Lin B, Wong KY, Hu C, Kokubo H, Pettitt BM. J Phys Chem Lett. 2011; 2:1626. [PubMed: 21765968]
100. Vazdar M, Pluharôvá E, Mason PE, Vácha R, Jungwirth P. J Phys Chem Lett. 2012; 3:2087.
101. Rankin BM, Hands MD, Wilcox DS, Fega KR, Slipchenko LV, Ben-Amotz D. Faraday Discuss. 2013; 160:255. [PubMed: 23795504]
102. Sala J, Guàrdia E, Martí J. Phys Chem Chem Phys. 2012; 14:10799. [PubMed: 22743694]
103. Caleman C, Hub JS, van Maaren PJ, van der Spoel D. Proc Nat Aca Sci. 2011; 108:6838.
104. Netz RR, Horinek D. Annu Rev Phys Chem. 2012; 63:401. [PubMed: 22404593]
105. Hauxwell F, Pallas NR, Pethica BA. Langmuir. 1992; 8:602.
106. Cui D, Ou S, Peters E, Patel S. J Phys Chem B. 2014; 118:4490. [PubMed: 24701961]
107. Cui D, Ou SC, Patel S. J Phys Chem B. 2015; 119:164. [PubMed: 25536388]
108. Bogár F, Bartha F, Násztor Z, Fábián L, Leitgeb B, Dér A. J Phys Chem B ASAP. 201410.1021/jp502505c
109. Feig M, Pettitt BM. Biophy J. 1999; 77:1769.
110. Liu P, Harder E, Berne BJ. J Phys Chem B. 2005; 109:2949. [PubMed: 16851308]
111. Kuffel A, Zielkiewicz J. J Phys Chem B. 2012; 116:12113. [PubMed: 22998120]
112. Godec A, Smith JC, Merzel F. Phys Rev Lett. 2011; 107:267801. [PubMed: 22243182]
113. Davis JG, Gierszal KP, Wang P, Ben-Amotz D. Nature Lett. 2012; 491:582.
114. Li JL, Car R, Tang C, Wingreen NS. Proc Nat Aca Sci. 2007; 104:2626.

115. Giovambattista N, Rossky PJ, Debenedetti PG. J Phys Chem B. 2009; 113:13723. [PubMed: 19435300]
116. Kumar P, Buldyrev SV, Starr FW, Giovambattista N, Stanley HE. Phys Rev E. 2005; 72:051503.
117. Mosaddeghi H, Alavi S, Kowsari MH, Najafi B. J Chem Phys. 2012; 137:184703. [PubMed: 23163385]
118. Corradini D, Rovere M, Gallo P. J Phys Chem B. 2011; 115:1461. [PubMed: 21268621]
119. Mancinelli R, Botti A, Bruni F, Riccia MA, Soper AK. Phys Chem Chem Phys. 2007; 9:2959. [PubMed: 17551619]
120. Galamba N. J Phys Chem B. 2012; 116:5242. [PubMed: 22480309]
121. Giovambattista N, Rossky PJ, Debenedetti PG. Phys Rev E. 2006; 73:041604.
122. Huang Z, Salim T, Brawley A, Patterson J, Matthews KS, Bondos SE. Adv Functional Matt. 2011; 21:2633.
123. Okazaki K, Sato T, Takano M. J Am Chem Soc. 2012; 134:8918. [PubMed: 22559201]
124. Wuttkea R, Hofmann H, Nettels D, Borgia MB, Mittal J, Best RB, Schuler B. Proc Nat Aca Sci. 2014; 111:5213.
125. Friedman R, Nachliel E, Gutman M. Biophy J. 2005; 89:768.
126. Wang J, Bratko D, Luzar A. Proc Nat Aca Sci. 2011; 108:6374.
127. Patel AJ, Varilly P, Jamadagni SN, Hagan MF, Chandler D, Garde S. J Phys Chem B. 2012; 116:2498. [PubMed: 22235927]
128. Giovambattista N, Debenedetti P, Rossky P. J Phys Chem C. 2007; 111:1323.
129. Willard A, Chandler D. Faraday Discuss. 2009; 141:209. [PubMed: 19227358]
130. Cui D, Ou S, Patel S. Proteins: Structure, Function and Bioinformatics. 2014; 82:1453.
131. Humphrey W, Dalke A, Schulten K. J Mol Graph. 1996; 14:33. [PubMed: 8744570]

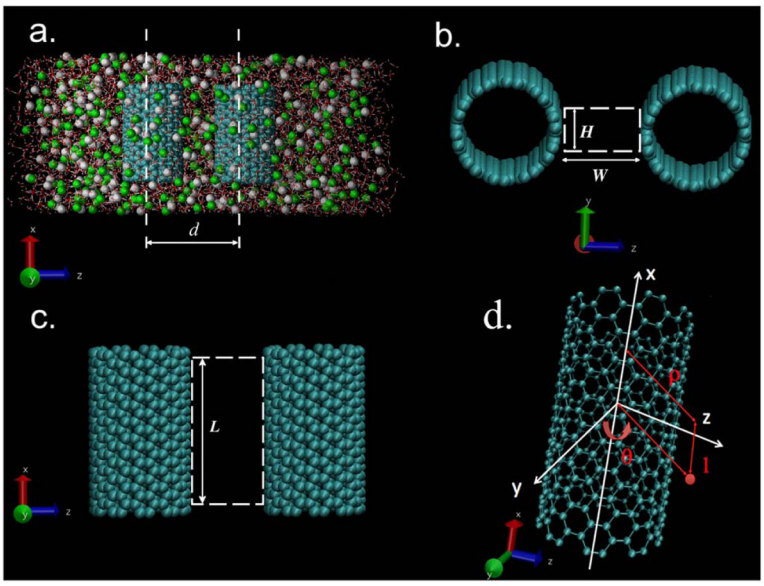

Figure 1.

Representative snapshots of the 3 m NaI system used in this study; separation (*d*) is 26.0 Å, which is defined by the distance between the center axes of the tubes. The diameter (*D*) and the length (*l*) of each tube are 13.56 Å and 24.0 Å, respectively. Atom types can be distinguished by the following color code: O (red), H (white), I^- (green), Na^+(gray), tube atoms (blue). (a) Side profile showing the relative solvation of the tubes in the normal and lateral directions. Projection of unsolvated tubes on (b) *y*–*z* and (c) and *x*–*z* plane. Dashed rectangular boxes in (b) and (c) define the confined region used in following analysis. The definition of the dimensionalities (*L*, *W*, *H*) is given in the text. (d) Illustration of grid points for fluctuation analyses using cylindrical coordinates. Snapshots are visualized using Visual Molecular Dynamics (VMD) program[131].

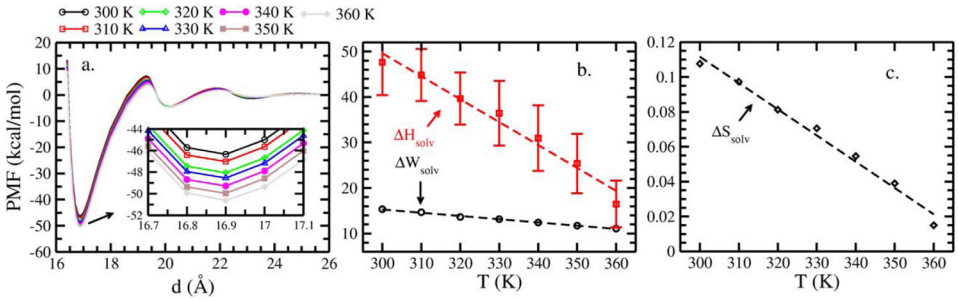

Figure 2.

(a) Total potential of mean force for tube association in 3 m NaI solutions under different temperatures. The inset shows the minimum region of the profiles. (b)(c) The values of solvent-induced Δ*W*, Δ*H* and Δ*S* for association as functions of the temperature. The unit for *y*-axis in panel (a) and (b) is kcal/mol; for panel (c) it is kcal/mol/K.

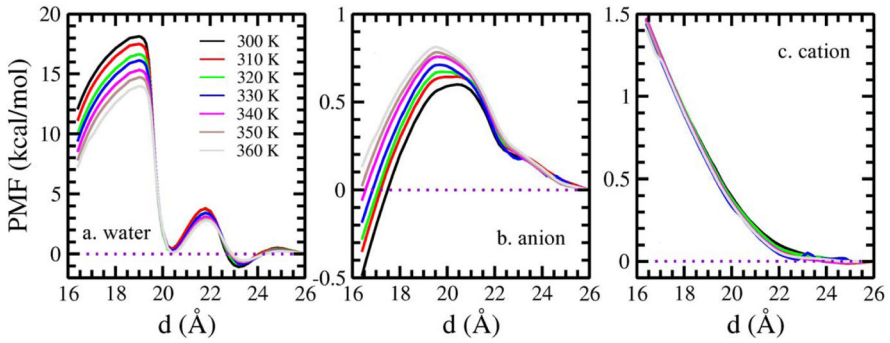

Figure 3.
Decomposition of PMF into (a) water (b) anion (c) cation contributions.

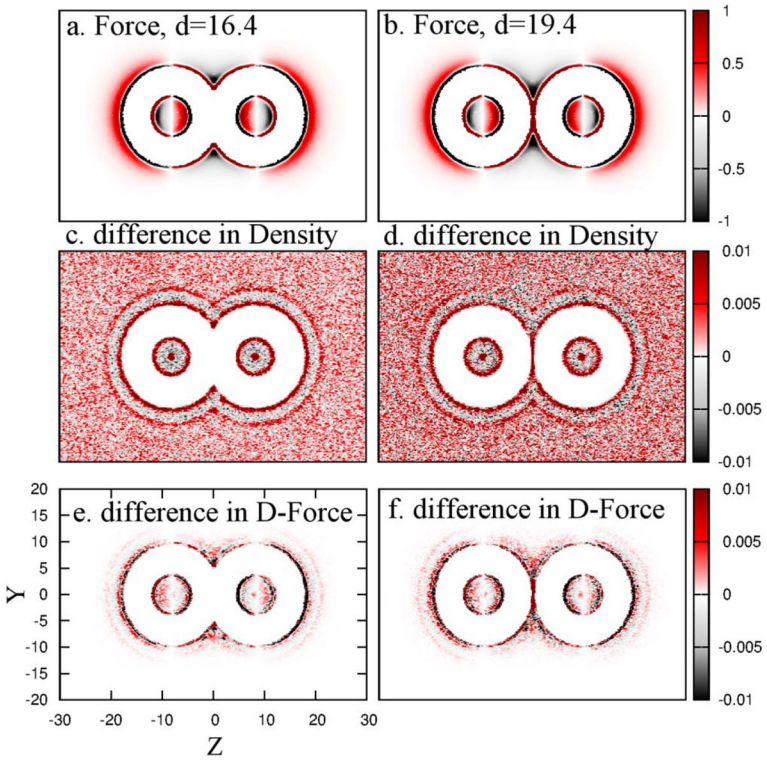

Figure 4.

The *z*-component of total forces from water molecules applied on the carbon nanotubes at position (*y*, *z*) in NaI solution, for the intertube separation *d* = (a) 16.4 (b) 19.4 Å. Panel (c) and (d) show the difference of density of water oxygen at location (*y*, *z*) around the carbon nanotubes between 300 K and 360 K, at the corresponding intertube separations. (e) and (f) illustrates the difference of density-weighted force at location (*y*, *z*) between 300 K and 360 K.

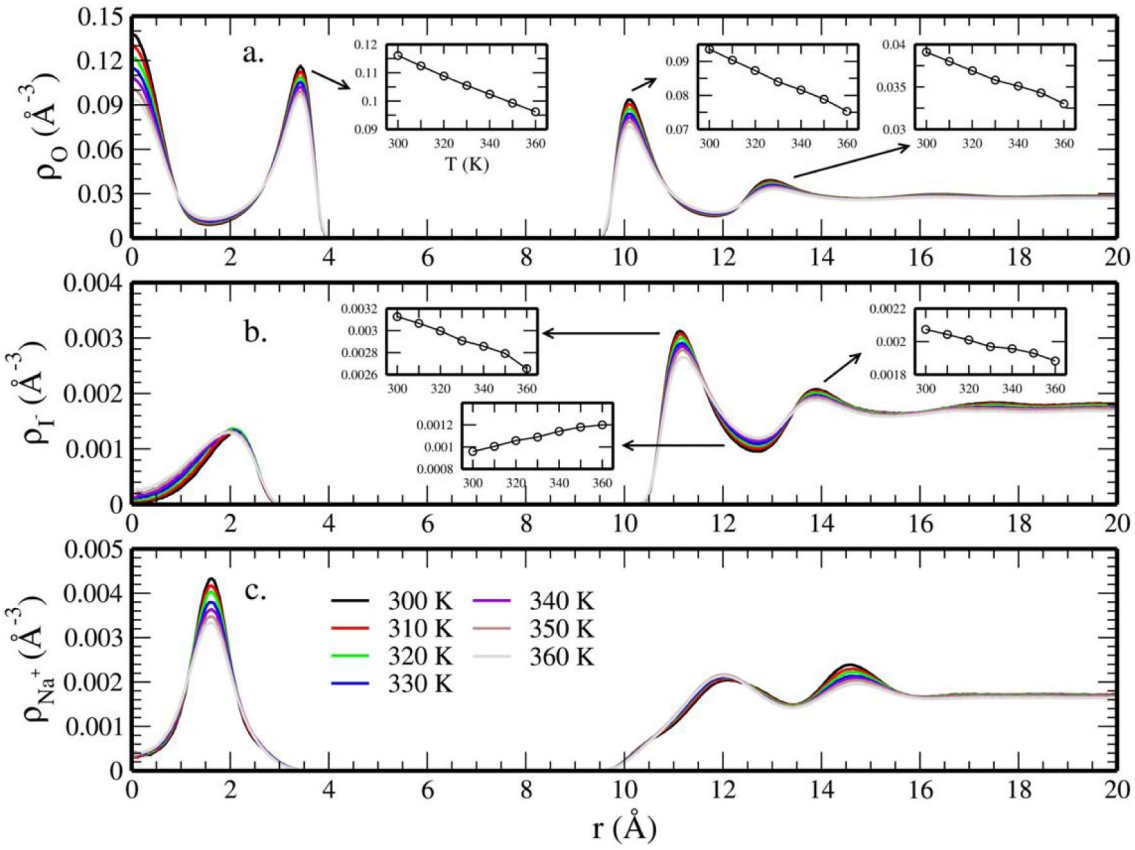

Figure 5.

Radial number density profiles of (a) water molecules (b) anions (c) cations at d = 16.4 Å under different temperatures. Insets focus on the maximum/minimum values versus temperature.

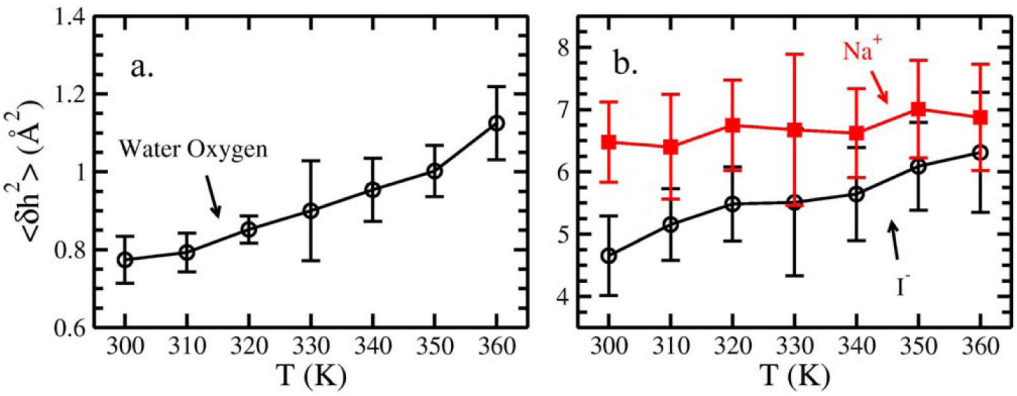

Figure 6.

Surface fluctuations (side facing the bulk) for (a) tube-water (b) tube-ion surface in 3 m NaI solution at different temperatures. Only $\langle \delta h^2(\theta, I) \rangle$ has -5 Å $\leq h \leq 5$ Å and $85° \leq \theta \leq 95°$ is used for the plotted value.

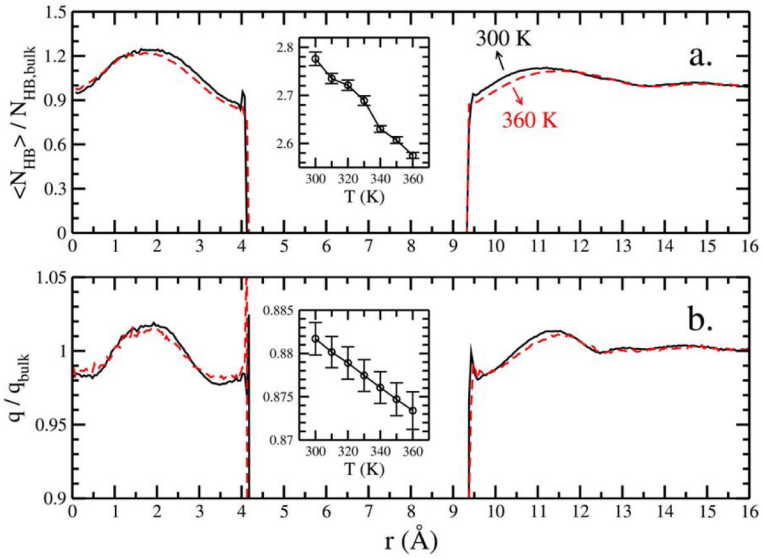

Figure 7.

(a) Hydrogen bonds (N_{HB}) (b) tetrahedral configuration parameter (q) of water molecules as functions of r.

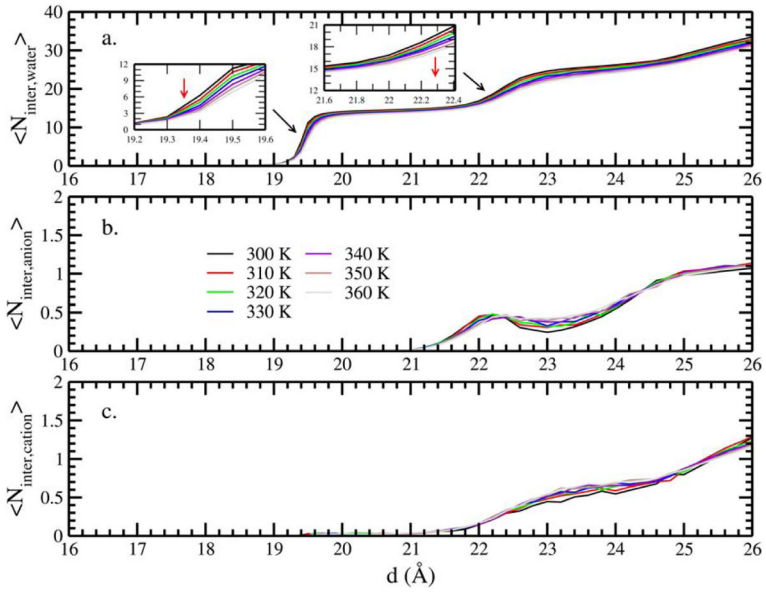

Figure 8.

Average number of (a) water molecules, (b) anions, and (c) cations of the confined region in pure water and 3 m NaI solutions. Insets show focused view of the jump of quantities. Red arrows in the insets indicate from low temperature to high temperature.

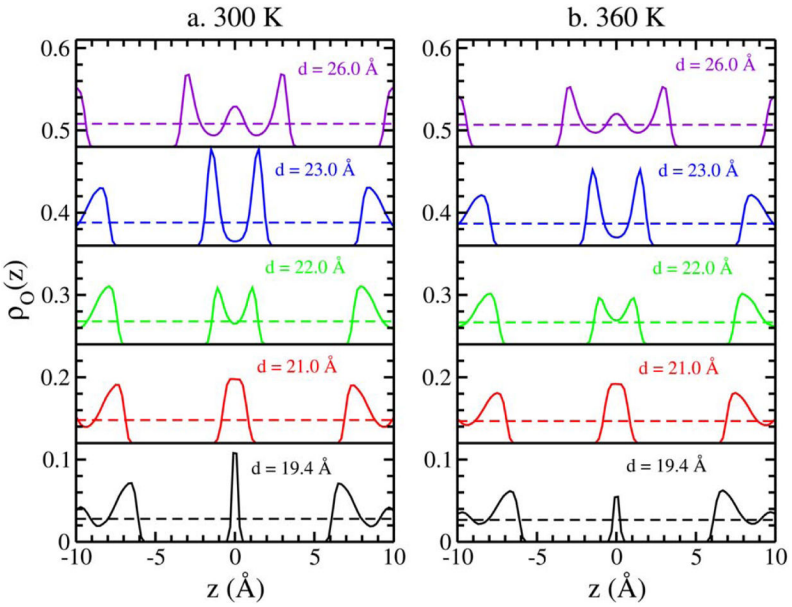

Figure 9.

Intertube tube-water surface fluctuations. Only $\langle \delta h^2(\theta, l) \rangle$ has -5 Å $\leq h \leq 5$ Å and $-95° \leq \theta \leq -85°$ is used for the plotted value. Red dashed lines indicate the fluctuation values for the sides facing the solvent bulk, along with the uncertainties (as plotted with the dotted lines).

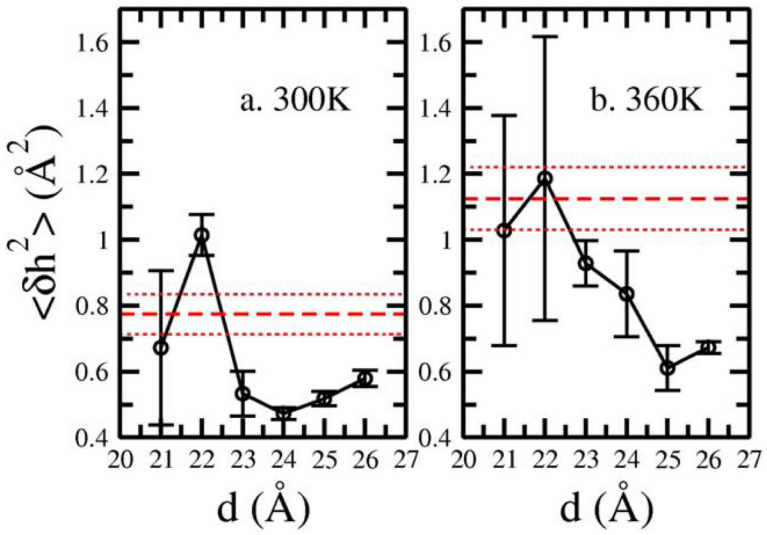

Figure 10.

Intertube tube-water surface fluctuations. Only $\langle \delta h^2(\theta, l) \rangle$ has -5 Å $\leq h \leq 5$ Å and $-95° \leq \theta \leq -85°$ is used for the plotted value. Red dashed lines indicate the fluctuation values for the sides facing the solvent bulk, along with the uncertainties (as plotted with the dotted lines).

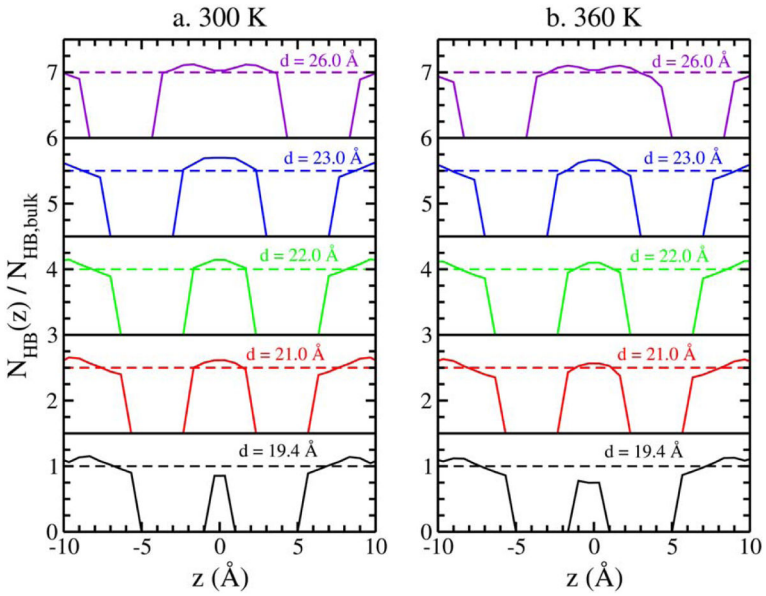

Figure 11.

Normalized hydrogen bond profiles for (a) 300 K and (b) 360 K along *z*-axis at intertube region. A vertical offset of 1.5 is added for clarity.

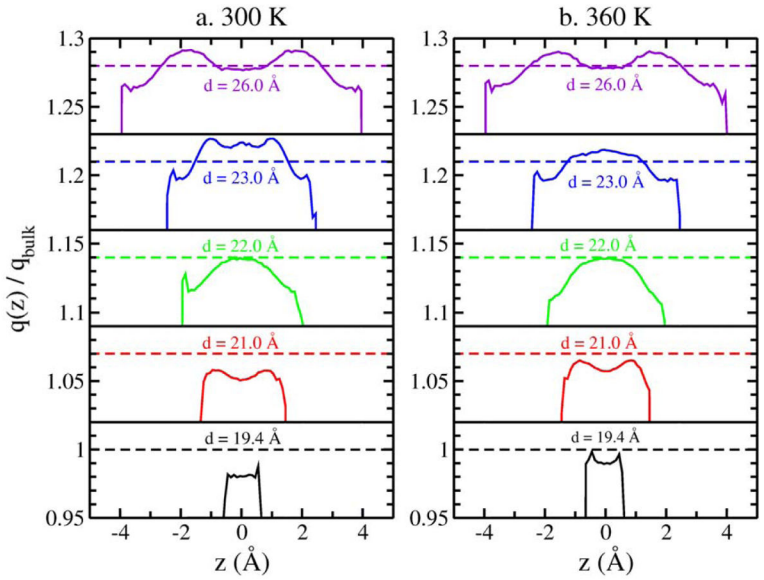

Figure 12.

Tetrahedral configuration parameter (q) for (a) 300 K and (b) 360 K along z-axis at intertube region. A vertical offset of 0.07 is added for clarity.

Table 1

Parameters used in the simulation.

	R_{min} (Å)	ε (kcal/mol)	q(e)
O	3.5537	0.1554	−0.8476
I^-	5.9872	0.0377	−1
Na^+	2.9004	0.1	1
Tube[a]	4.0195	0.0663	0

[a]The LJ parameters for oxygen-tube interaction are fixed to be ε_{ij} = 0.1015 kcal/mol, R_{min} = 3.7793 Å.

Table 2

Decomposition of potential of mean force into contributions from water, tubes, anions, and cations. ΔW^b refers to the values at the first barrier. All values for ΔW are calculated using Equation 5 and are expressed in kcal/mol.

System	ΔW_{tube}	ΔW_{water}	ΔW_{anion}	ΔW_{cation}	ΔW_{total}	ΔW^b
300 K	−61.69	14.31	−0.25	1.28	−46.35	7.26
310 K	−61.69	13.51	−0.13	1.29	−47.02	6.77
320 K	−61.69	12.41	−0.072	1.30	−48.07	5.94
330 K	−61.69	11.81	0.021	1.28	−48.58	5.50
340 K	−61.69	10.99	0.13	1.29	−49.28	4.85
350 K	−61.69	10.25	0.21	1.27	−49.97	4.29
360 K	−61.69	9.56	0.29	1.23	−50.61	3.85

Table 3

Average number of water molecules, anions and cations within the tube. Values in parentheses denote the uncertainties in the last reported digit as determined from the standard deviations.

System	$\langle N_{\text{intra–tube,water}} \rangle$	$\langle N_{\text{intra–tube,anion}} \rangle$	$\langle N_{\text{intra–tube,cation}} \rangle$
300 K	51.96(27)	0.42(7)	1.05(8)
310 K	50.16(20)	0.45(6)	1.05(7)
320 K	49.41(19)	0.45(4)	1.03(5)
330 K	48.66(21)	0.47(5)	1.01(5)
340 K	47.92(19)	0.48(4)	0.99(5)
350 K	47.20(18)	0.48(4)	0.96(5)
360 K	46.45(19)	0.49(4)	0.94(5)

Table 4

Features of the intertube water densities in Figure 9. The units for $\rho_{o,max}$ and $\rho_{o,min}$ are $Å^{-3}$.

System	$\rho_{o,max}$	$\rho_{o,min}$	$\rho_{o,max}/\rho_{o,min}$
300 K			
d = 22.0 Å	0.069	0.025	2.76
d = 23.0 Å	0.117	0.005	22.76
360 K			
d = 22.0 Å	0.056	0.0029	1.94
d = 23.0 Å	0.092	0.0098	9.35